Seamless Switching and Grid Reconnection of Microgrid Using Petri Recurrent Wavelet Fuzzy Neural Network

Kuang-Hsiung Tan and Tzu-Yu Tseng

***Abstract*—A Petri recurrent wavelet fuzzy neural network (PetriRWFNN) controller and a simple presynchronization estimation are proposed for the operations of seamless switching and grid reconnection in a microgrid system. The microgrid using master/slave control consists of a storage system, photovoltaic (PV) system and loads, and can be operated in either grid-connected mode or islanded mode. Since the different control algorithm is adopted in the master distributed generator at different operation modes, the transient deterioration in voltage and active power output of the microgrid system is obvious during the mode switching. Moreover, when the microgrid is operated in islanded mode and the power grid returns to normal operation, the microgrid cannot directly reconnect with the power grid to avoid a large inrush of current and failed grid reconnection due to the asynchronous angle between the islanded microgrid and the grid angle. Therefore, a novel PetriRWFNN controller is proposed to improve the transient responses of the voltage and active power of the microgrid during mode switching. The network structure and the online learning algorithm of the proposed PetriRWFNN are introduced in detail. Furthermore, a simple and fast presynchronization estimation for grid reconnection during the switching from the islanded mode to the grid-connected mode is also proposed in this article. Finally, some experimental results are provided to certify the effectiveness and feasibility of the microgrid system using the proposed PetriRWFNN controller and presynchronization estimation for the operations of seamless switching and grid reconnection.**

***Index Terms*—Grid reconnection, microgrid, petri net, presynchronization, wavelet neural network.**

I. Introduction

RECENTLY, owing to the consciousness-raising of the environmental pollution and energy crisis and the advanced development in power electronic technologies, the distributed generators (DGs) using the renewable energy sources have been gotten significant attention [1]–[3]. Moreover, the conventional utility grid is in a centralized way in which the power plants are located in the remote districts [4]–[6]. Thus, the generated energies should be dispatched to the end client over large distances and through complicated transmission systems, including the various transformers [4]. The drawbacks of the power plants in such a centralized way are the reduced flexibility, the high transmission and distribution losses, and difficulty to meet the demand growth [5]. The probability of grid instabilities and power failure will be increased in the power system [4]. Hence, a novel concept of a power system has been arisen and denominated as a microgrid. The microgrid integrates the DGs and the loads at the customer side and can be operated in either grid-connected mode or islanded mode [2]. In other words, the microgrid is performed in a decentralized way and can provide the increased reliability and flexibility to its operation [5], [6]. Thus, the microgrid has been developed in many countries and areas. In terms of the control algorithm, the master/slave is the common method adopted in microgrid [2], [7]. In the master/slave control algorithm, one of the DGs in the microgrid is regarded as master DG and implements the active and reactive power controls in grid-connected mode. The rest of DGs are defined as a slave and also perform the active and reactive power controls in grid-connected mode. In the grid-connected mode, the voltage and frequency of the microgrid are maintained by the power grid. When the power grid is interrupted, the microgrid is operated in islanded mode. In this mode, owing to the absence of the power grid, the voltage and frequency of the microgrid are controlled by the master DG. The slave DGs still implement the active and reactive power controls in islanded mode [2], [7]. The advantages of the master/slave control algorithm are easy to implement technically and owns a relatively low risk [8]. However, the seamless switching between the grid-connected mode and the islanded mode is a challenge due to the different control algorithms at different operation modes, resulting in serious fluctuations of voltage and power flow [9], [10].

The seamless switching from islanded mode to grid-connected mode has another noteworthy task to investigate, namely presynchronization. Since the electric angle of the islanded microgrid and the grid angle are asynchronous, the microgrid cannot directly reconnect with the power grid to avoid a large inrush of current and failed grid reconnection [9]. Hence, many presynchronization methods have been proposed [9], [11]–[13]. The simplest method is to shut down all DGs of the microgrid before reconnecting with the grid. However,

Manuscript received November 11, 2020; revised January 20, 2021; accepted March 15, 2021. Date of publication March 18, 2021; date of current version June 30, 2021. This work was supported by the Ministry of Science and Technology of Taiwan under Grant MOST 109-3116-F-008-005. Recommended for publication by Associate Editor J. M. Guerrero. *(Corresponding author: Kuang-Hsiung Tan)*

Kuang-Hsiung Tan is with the Department of Electrical and Electronic Engineering, Chung Cheng Institute of Technology, National Defense University, Taoyuan 335, Taiwan (e-mail: s913115@gmail.com).

Tzu-Yu Tseng is with the Department of Electrical Engineering, National Central University, Chungli 320, Taiwan (e-mail: 40440134@gm.nfu.edu.tw).

Color versions of one or more figures in this article are available at https://doi.org/10.1109/TPEL.2021.3066986.

Digital Object Identifier 10.1109/TPEL.2021.3066986

the reliability and stability of the microgrid are poor due to the interruption of the DGs and load requirements. In [9], a synchronizer based on a bidirectional converter was proposed to generate the triggering signal for grid reconnection. The synchronizer adopted a correction factor and measured the system parameters, frequency, voltage, and phase difference between the microgrid and the grid sides to achieve the synchronization. However, since an additional bidirectional converter is adopted to synchronize with the grid, the structure is complex. Furthermore, a synchronization controller was proposed in [11]. The synchronization controller adopted the phase difference between the microgrid and grid voltages and two variables obtained by the three-phase voltages of the microgrid and power grid to compute the new phase angle for synchronization with the grid. However, a large amount of computation of this method is needed. In [12], an AND logic gate circuit and the voltage difference and the frequency difference between the microgrid and grid are proposed to implement the operation of the diesel generator and compare with the desired value. When the errors are within the desired range, the breaker for the grid-reconnection turns ON. Although the method is uncomplicated, it requires much time to synchronize with the grid. In addition, a phase-control compensator combined with the frequency error to generate the active power command for the synchronization was proposed in [13]. This method is still time-consuming. Thus, although many presynchronization methods have been proposed for grid reconnection in microgrid systems, the methods are either complex or time-consuming.

In general, the conventional proportional-integral (PI) controller is easy to be implemented and owns the advantage of simple structure. However, the PI controller is not robust in coping with the system uncertainties such as parameter variations, external disturbances, and modeling errors in real-world applications [14]. Moreover, the gains of the PI controller obtained by trial and error are not always suitable for different operating conditions [15]. Hence, intelligent controllers, such as fuzzy logic and artificial neural network, have been proposed to overcome the poor characteristic of the conventional PI controller in the past decades. Nowadays, fuzzy neural network (FNN) has been widely investigated in engineering applications due to the abilities of FNN in generalization, self-learning, parallel computation, and coping with uncertain nonlinear systems [16], [17]. The FNN using different learning algorithms for brushless dc motor drives was researched in [17]. In [18], a self-constructing FNN was proposed for a fault-tolerant aircraft control scheme against actuator faults. Moreover, the neural network using wavelet transform theory was first proposed by Zhang and Benveniste [19]. The wavelet neural network (WNN), which integrates the wavelet transform and neural network, has been researched in [20]–[22]. Owing to the property of wavelet decomposition, the WNN possesses the capabilities of pattern classification, fault tolerance, approximation, and quick convergence [21]. In [23], a WNN recognition system has been proposed for personal fitness assistance and elderly daily activity monitoring applications. Furthermore, Petri net (PN) was developed as a net-like mathematical tool for the study of communication with automata [23]. The PN owns the graphical, analytical, and mathematical modeling abilities [24]. Thus, the

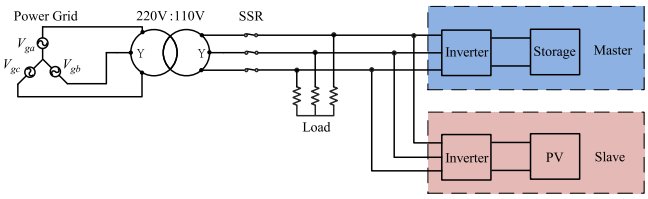

Fig. 1. System configuration of a microgrid.

PN is a superior tool for the specification and verification of concurrent, parallel, distributed, asynchronous, and uncertain information processing systems. In addition, a recurrent neural network (RNN) uses feedback connections to memorize the temporal characteristics of an incoming dataset [25]. Hence, RNN is more powerful than the conventional feedforward network and is suitable to model nonlinear dynamic systems due to the memory characteristic [25], [26]. A video-based person reidentification system using RNN for wide-area tracking was proposed in [27]. In [28], a sequence learning model based on RNN to predict taxi demand in different areas of a city was proposed. Therefore, in this article, according to the above merits of FNN, WNN, RNN, and PN, a novel Petri recurrent wavelet fuzzy neural network (PetriRWFNN) intelligent controller is first proposed.

In this article, an ac microgrid using master/slave control is proposed. The microgrid comprises a storage system, PV system and loads, and can be operated in either grid-connected mode or islanded mode. Since the different control algorithm is adopted in the master DG at different operation modes, the transient deterioration in voltage and active power output of the microgrid system is obvious during the mode switching [9], [10]. Moreover, although many presynchronization methods have been proposed in the works of literature for grid reconnection in microgrid systems, the methods are either complex or time-consuming. Therefore, in this article, a novel PetriRWFNN controller is proposed to replace the conventional PI controller for improving the transient responses of the voltage and active power of the microgrid during mode switching. Furthermore, a simple and fast presynchronization estimation for grid reconnection during the switching from the islanded mode to grid-connected mode is also proposed. The operating theories of the microgrid using master/slave control will be represented in Section II. Then, the network structure, online learning based on the backpropagation (BP) algorithm, and convergence analysis of the proposed PetriRWFNN controller are described detailedly in Section III. Furthermore, some experimental results to verify the effectiveness and feasibility of the microgrid system using the proposed PetriRWFNN controller for the operations of seamless switching and grid reconnection are demonstrated in Section IV. Finally, the conclusions will be given in Section V.

II. Operating Theories of Microgrid

In this article, the system configuration of a microgrid is shown in Fig. 1. The microgrid is composed of a storage system, PV system, and three-phase resistive loads. The storage system is regarded as master DG and the PV system is regarded as a slave unit. The line-to-line voltage of the microgrid is 110 Vrms.

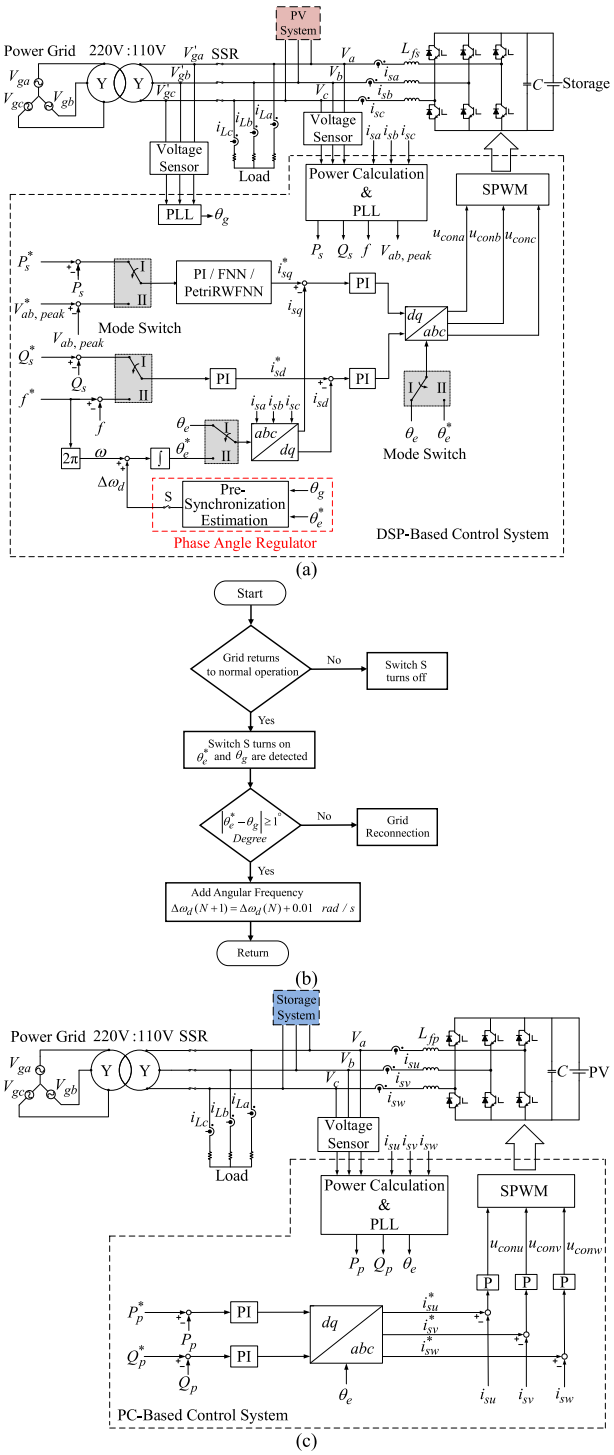

Fig. 2. Schematic of ac microgrid using master/slave algorithm and presynchronization estimation. (a) Control block of the storage system. (b) Flowchart of phase angle regulator for presynchronization estimation. (c) Control block of the PV system.

Moreover, the microgrid is connected with the power grid via a static switch relay (SSR) and a step-up transformer with a turn ratio of 2 to transfer the voltage to a 220 Vrms distributed network. Furthermore, the schematic of the developed ac microgrid using master/slave algorithm and presynchronization estimation is provided in Fig. 2.

A. Control Algorithm and Presynchronization Estimation of Master DG

The control block of the storage system regarded as master DG is represented in Fig. 2(a). In Fig. 2(a), the control algorithm of the storage system is split into two operation modes. In mode I, the storage system is in parallel with the power grid. In other words, the microgrid is operated in grid-connected mode. In grid-connected mode, the voltage and frequency of the microgrid are imposed by the power grid. Thus, the storage system has adopted the active power and reactive power control in mode I. First, for the purpose of the synchronization with the power grid, the three-phase voltages V_a, V_b, V_c of the microgrid are detected and the dq-axis voltages V_d and V_q of the microgrid can be computed by using abc/dq coordinate transformation in the following:

$$\begin{bmatrix} V_q \\ V_d \end{bmatrix} = \frac{2}{3}\begin{bmatrix} \cos\theta_e & -\sin\theta_e \\ \sin\theta_e & \cos\theta_e \end{bmatrix}\begin{bmatrix} 1 & -\frac{1}{2} & -\frac{1}{2} \\ 0 & -\frac{\sqrt{3}}{2} & \frac{\sqrt{3}}{2} \end{bmatrix}\begin{bmatrix} V_a \\ V_b \\ V_c \end{bmatrix}. \tag{1}$$

Then, the synchronous angle θ_e is gained by using the phase-locked loop (PLL). Moreover, to calculate the output active power and reactive power of the storage system, the three-phase currents i_{sa}, i_{sb}, i_{sc} of the storage system are detected and the dq-axis currents i_{sd} and i_{sq} of the storage system can be obtained as follows:

$$\begin{bmatrix} i_{sq} \\ i_{sd} \end{bmatrix} = \frac{2}{3}\begin{bmatrix} \cos\theta_e & -\sin\theta_e \\ \sin\theta_e & \cos\theta_e \end{bmatrix}\begin{bmatrix} 1 & -\frac{1}{2} & -\frac{1}{2} \\ 0 & -\frac{\sqrt{3}}{2} & \frac{\sqrt{3}}{2} \end{bmatrix}\begin{bmatrix} i_{sa} \\ i_{sb} \\ i_{sc} \end{bmatrix}. \tag{2}$$

Thus, according to (1) and (2), the output active power P_s and output reactive power Q_s of the storage system are obtained through the power calculation

$$P_s = \frac{3}{2}(V_q i_{sq} + V_d i_{sd}) \tag{3}$$

$$Q_s = \frac{3}{2}(V_q i_{sd} - V_d i_{sq}). \tag{4}$$

By means of the PLL, assuming that the current vector in phase with the voltage resulted in $V_d = 0$ [7], the output active power P_s and output reactive power Q_s of the storage system are rewritten as follows:

$$P_s = \frac{3}{2}V_q i_{sq} \tag{5}$$

$$Q_s = \frac{3}{2}V_q i_{sd}. \tag{6}$$

Hence, the output active power P_s and output reactive power Q_s of the storage system will be proportional to i_{sq} and i_{sd} currents, respectively. Moreover, the q-axis current command i^*_{sq} is regulated by the conventional PI, FNN, or the proposed PetriRWFNN controller using the difference between the active power command P^*_s and the active power P_s as input. The d-axis current command i^*_{sd} is obtained by the conventional PI controller using the reactive power error as input. Then, the dq-axis current commands i^*_{sq} and i^*_{sd} are compared with the dq-axis currents i_{sq} and i_{sd} to obtain the control signals u_{cona}, u_{conb}, u_{conc} for the

generation of the sinusoidal pulsewidth modulation (SPWM) switching signals. On the other hand, when the power grid is interrupted, the microgrid can promptly disconnect from the power grid via the SSR and smoothly switch the operation mode from mode I to II. In mode II, namely islanded mode, since the absence of the power grid, the voltage and frequency of the microgrid should be maintained by the storage system. Thus, the control algorithm of the storage system is changed from active power and reactive power control in mode I to voltage and frequency control in mode II. In islanded mode, according to the PLL algorithm, the peak value of the line-to-line voltage $V_{ab,\text{peak}}$ and the frequency f of the microgrid are computed. Moreover, the q-axis current command i_{sq}^* for voltage control is gained via the conventional PI, FNN, or the proposed PetriRWFNN controller using the voltage error as input. The d-axis current command i_{sd}^* for frequency control is obtained by the conventional PI controller using the frequency error as input. Furthermore, the electric angle command θ_e^* for the abc/dq and dq/abc coordinate transformations can also be calculated by using the frequency command f^*

$$\theta_e^* = \int \omega^* dt = 2\pi \int f^* dt \tag{7}$$

where ω^* is the angular frequency. Finally, the SPWM switching signals are gained for the voltage and frequency control of the storage system operated in islanded mode.

When the microgrid is operated in islanded mode and the power grid returns to normal operation, the microgrid should be reconnected with the power grid. However, since the electric angle command θ_e^* of the microgrid and the grid angle θ_g are asynchronous, the microgrid cannot directly reconnect with the power grid to avoid a large inrush of current and failed grid reconnection [9]. Thus, a simple and fast presynchronization estimation for grid reconnection from the islanded mode to grid-connected mode is proposed. The flowchart of the phase angle regulator for presynchronization estimation is represented in Fig. 2(b). First, when the power grid returns to the normal operation, the switch S showed in Fig. 2(a) turns ON and the electric angle θ_e^* of the microgrid operated in islanded mode is compared with the detected grid angle θ_g. When the absolute value of the angular error is larger than 1°, a slight amount of angular frequency $\Delta\omega_d$ is added to the original angular frequency ω to decrease the angular error. As long as the angular error is less than 1°, the electric angle θ_e^* of the microgrid and the grid angle θ_g are regarded as synchronization. Hence, the microgrid can reconnect with the power grid through the SSR and change the operation mode and control algorithm shown in Fig. 2(a).

Comparing to [2], since the purpose and control scheme of the storage system are different from this article, the performances of the storage system are also different. In [2], since the dynamic responses of the inverter-based DGs are much faster than the conventional synchronous generator (SG), which will make the power system susceptible to oscillation resulting from sudden load variations, the swing equation of SG is added to the storage system to track the active power command smoothly to overcome the drawbacks of traditional inverter-based DGs for lack of inertia. Moreover, an online trained recurrent probabilistic wavelet fuzzy neural network (RPWFNN) is proposed to replace the PI controller in the storage system for improving the transient and steady-state responses of voltage control in the microgrid operated in islanded mode during the load variation. Furthermore, the issue of the microgrid switching from islanded mode to grid-connected mode is not solved in [2]. On the other hand, in this article, to achieve the operations of seamless switching and grid reconnection in a microgrid system, a simple and fast presynchronization estimation for grid reconnection during the switching from islanded mode to grid-connected mode is proposed.

B. Control Algorithm of Slave DG

The control block of the PV system, regarded as slave DG, is illustrated in Fig. 2(c). The PV system adopts active power and reactive power control in both the grid-connected mode and islanded mode. First, the three-phase voltages $V_a,\ V_b,\ V_c$ of the microgrid and the three-phase currents $i_{su},\ i_{sv},\ i_{sw}$ of the PV system are measured. Then, the output active power P_p and output reactive power Q_p of the PV system are gained through the power calculation and PLL units. Moreover, the three-phase current commands $i_{su}^*,\ i_{sv}^*,\ i_{sw}^*$ are obtained by PI controllers using the active and reactive power errors as inputs through dq/abc coordinate transformation. Finally, the three-phase currents $i_{su},\ i_{sv},\ i_{sw}$ are compared with the three-phase current commands $i_{su}^*,\ i_{sv}^*,\ i_{sw}^*$ to compute the control signals $u_{conu},\ u_{conv},\ u_{conw}$ through P controllers for the generation of SPWM switching signals of the PV system.

III. Intelligent PetriRWFNN Controller

Since the mode switching between the grid-connected mode and islanded mode will cause the transient deterioration in voltage and active power output of the microgrid system [9], [10], a novel PetriRWFNN controller is proposed in this article to replace the conventional PI controller for improving the transient responses of the voltage and active power of the microgrid system during the mode switching. The proposed PetriRWFNN controller is composed of an input layer, membership layer, rule layer, Petri layer, wavelet and consequent layer, and output layer. Moreover, the network structure of the proposed PetriRWFNN is illustrated in Fig. 3(a). The detailed network structure and online learning algorithm of the proposed PetriRWFNN controller are represented in the following.

A. Network Structure

1) Input Layer: The signal propagation of this layer is depicted as follows:

$$\text{net}_i^1(N) = x_i^1 \tag{8}$$

$$y_i^1(N) = f_i^1(\text{net}_i^1(N)) = \text{net}_i^1(N), i = 1, 2 \tag{9}$$

where N denotes the Nth iteration; $x_1^1 = e(t)$; $x_2^1 = \dot{e}(t)$. The input variables of the proposed PetriRWFNN are $e(t) = P_s^*(t) - P_s(t)$ for the active power control of the storage system operated in mode I or $e(t) = V_{ab,\text{peak}}^*(t) - V_{ab,\text{peak}}(t)$ for voltage control

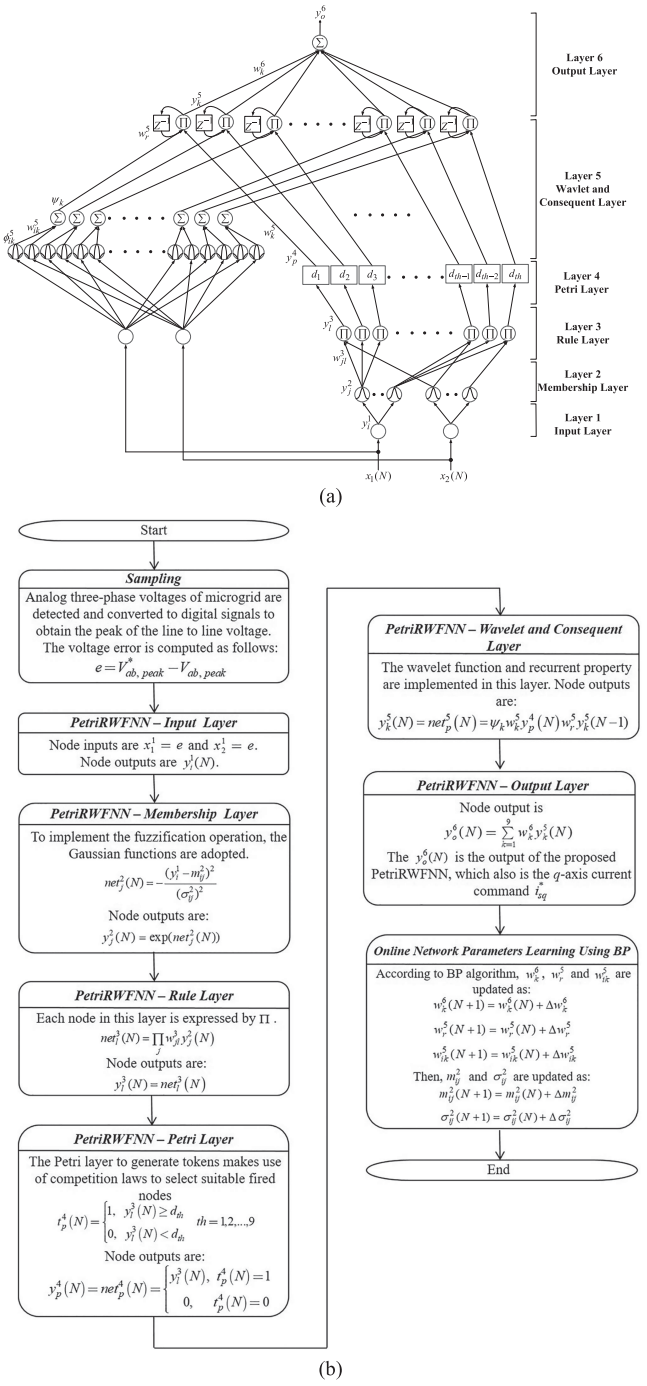

Fig. 3. PetriRWFNN controller. (a) Network structure. (b) Flowchart of storage using the proposed PetriRWFNN controller for voltage control in islanded mode.

of the storage system operated in mode II and its derivative $x_2^1 = \dot{e}(t)$.

2) Membership Layer: Each node in this layer utilizes a Gaussian function to implement the fuzzification operation. For the *j*th node

$$\mathrm{net}_j^2(N) = -\frac{\left(y_i^1 - m_{ij}^2\right)^2}{\left(\sigma_{ij}^2\right)^2} \tag{10}$$

$$y_j^2(N) = f_j^2(\mathrm{net}_j^2(N)) = \exp(\mathrm{net}_j^2(N)), j = 1, 2, \ldots, 6 \tag{11}$$

where m_{ij}^2 and σ_{ij}^2 represent, respectively, the mean and the standard deviation of the Gaussian function in the *j*th term input linguistic variable y_i^1 to the node of membership layer.

3) Rule Layer: Each node in this layer is expressed by $\prod$, which multiplies the input signals and outputs the result of the product

$$\mathrm{net}_l^3(N) = \prod_j w_{jl}^3 y_j^2(N) \tag{12}$$

$$y_l^3(N) = f_l^3\left(\mathrm{net}_l^3(N)\right) = \mathrm{net}_l^3(N), l = 1, 2, \ldots, 9 \tag{13}$$

where w_{jl}^3 is the connective weight between the membership layer and the rule layer which is set to be 1; y_j^2 is the *j*th input to the node of rule layer.

4) Petri Layer: The Petri layer of the proposed PetriRWFNN to generate tokens makes use of competition laws to select suitable fired nodes in this article [29]. When the token is produced in the input place, the transition is in enable state. Then, the transition is fired or unfired according to the following equations:

$$t_p^4(N) = \begin{cases} 1, \mathrm{y}_l^3(N) \geq d_{\mathrm{th}} \\ 0, \mathrm{y}_l^3(N) < d_{\mathrm{th}} \end{cases} \mathrm{th} = 1, 2, \ldots, 9 \tag{14}$$

$$d_{th} = \frac{\alpha \exp(-\beta V)}{1 + \exp(-\beta V)} \tag{15}$$

where d_{th} is the dynamic threshold value and is varied by the error function $V = (e + \dot{e})/2$ [29]; $t_p^4(\mathrm{N})$ is the transition; α and β are positive constants and set to be 0.23 and 3, respectively, by empirical rules. When the transition is unfired, the token will stay in the input place. In other words, when the transition is fired, the tokens are removed from their input place to output place. Therefore, the input and output of this layer can be described in the following:

$$\mathrm{net}_p^4(N) = \begin{cases} \mathrm{y}_l^3(N), t_p^4(N) = 1 \\ 0, t_p^4(N) = 0 \end{cases} \tag{16}$$

$$y_p^4(N) = f_p^4\left(\mathrm{net}_p^4(N)\right) = \mathrm{net}_p^4(N), p = 1, 2, \ldots, 9. \tag{17}$$

5) Wavelet and Consequent Layer: The wavelet function and the recurrent property of RNN are implemented in this layer. The wavelet function is expressed as follows:

$$\phi_{ik}^5(x) = \frac{1}{\sqrt{|\sigma_{ik}^5|}}\left[1 - \frac{\left(x_i^1(N) - m_{ik}^5\right)^2}{\left(\sigma_{ik}^5\right)^2}\right] \exp\left[-\frac{\left(x_i^1(N) - m_{ik}^5\right)^2}{2\left(\sigma_{ik}^5\right)^2}\right]$$
$$i = 1, 2; k = 1, 2, \ldots, 9 \tag{18}$$

$$\psi_k(N) = \sum w_{ik}^5 \phi_{ik}^5(x) \tag{19}$$

where w_{ik}^5 is the wavelet weight; ϕ_{ik}^5 is the *i*th in the *k*th term wavelet output to the node of wavelet sum layer; $\psi_k(N)$ is the consequence of wavelet function. Moreover, the input and

output of the wavelet and consequent layer can be represented as follows:

$$\text{net}_k^5(N) = \psi_k w_k^5 y_p^4(N)\, w_r^5 y_k^5(N-1), k = 1, 2, \ldots, 9 \quad (20)$$

$$y_k^5(N) = f_k^5(\text{net}_k^5(N)) = \text{net}_p^5(N) \quad (21)$$

where w_r^5 is the connective weight of the node to implement the recurrent property; w_k^5 is the connective weight between the wavelet and consequent layer and the Petri layer, which is set to be 1; $y_k^5(N)$ is the output of this layer. Furthermore, since the RNN is more powerful than the traditional feedforward network, the recurrent property of the proposed PetriRWFNN is computed in (20). The recurrent property is to adopt feedback connection to memorize the temporal characteristic of an incoming dataset. Hence, the recurrent connection endows the network with memory [25].

6) Output Layer: The relationship of the input and output of this layer is depicted in the following:

$$\text{net}_o^6(N) = \sum_{k=1}^{9} w_k^6 y_k^5(N), o = 1 \quad (22)$$

$$y_o^6(N) = f_o^6(\text{net}_o^6(N)) \quad (23)$$

where w_k^6 are the connective weights between the output layer and the wavelet and consequent layer; $y_o^6(N)$ is the output of the proposed PetriRWFNN, which is also the q-axis current command i_{sq}^* shown in Fig. 2(a) for the active power control in mode I and voltage regulation control in mode II of the storage system.

B. Online Learning

The BP algorithm is adopted for the online learning of the proposed PetriRWFNN in this article. The BP algorithm online trains the parameters of the proposed PetriRWFNN to match input set to an output set by means of the partial derivatives of each parameter to an error function E [17]. In this article, the error function E is defined as the following equation for the online learning algorithm using a supervised gradient descent method:

$$E(N) = \frac{1}{2}\left(V_{ab,\text{peak}}^* - V_{ab,\text{peak}}\right)^2 = \frac{1}{2}e^2. \quad (24)$$

The detailed procedure of the learning algorithm of the proposed PetriRWFNN is introduced in the following.

1) *Output Layer:* In this layer, the propagated error term is given in the following:

$$\delta_o^6 = -\frac{\partial E}{\partial y_o^6(N)} = -\frac{\partial E}{\partial V_{ab,\text{peak}}}\frac{\partial V_{ab,\text{peak}}}{\partial y_o^6(N)}. \quad (25)$$

The connective weight is calculated and updated as follows by using the chain rule:

$$\Delta w_k^6 = -\eta_1 \frac{\partial E}{\partial w_k^6} = -\eta_1 \frac{\partial E}{\partial y_o^6(N)}\frac{\partial y_o^6(N)}{\partial w_k^6} = \eta_1 \delta_o^6 y_k^5 \quad (26)$$

where η_1 is the learning rate. The connective weight w_k^6 can be updated as

$$w_k^6(N+1) = w_k^6(N) + \Delta w_k^6. \quad (27)$$

2) *Wavelet and Consequent Layer:* The error terms of this layer to be propagated are given as

$$\delta_k^5 = -\frac{\partial E}{\partial y_k^5(N)} = -\left[\frac{\partial E}{\partial y_o^6(N)}\right]\frac{\partial y_o^6(N)}{\partial y_k^5} = \delta_o^6 w_k^6 \quad (28)$$

$$\delta_{ik}^5 = -\frac{\partial E}{\partial \psi_k} = -\left[\frac{\partial E}{\partial y_o^6(N)}\frac{\partial y_o^6(N)}{\partial y_k^5(N)}\right]\frac{\partial y_k^5(N)}{\partial \psi_k(N)} = \delta_k^5 w_k^5 y_p^4 w_r^5 y_k^5(N-1). \quad (29)$$

The updates of the connective weights Δw_r^5 and Δw_{ik}^5 are obtained by using the chain rule

$$\Delta w_r^5 = -\eta_2 \frac{\partial E}{\partial w_r^5} = -\eta_2\left[\frac{\partial E}{\partial y_o^6(N)}\frac{\partial y_o^6(N)}{\partial y_k^5(N)}\right]\frac{\partial y_k^5(N)}{\partial w_r^5(N)} = \eta_2 \delta_k^5 \psi_k w_k^5 y_p^4 y_k^5(N-1) \quad (30)$$

$$\Delta w_{ik}^5 = -\eta_3 \frac{\partial E}{\partial w_{ik}^5} = -\eta_3\left[\frac{\partial E}{\partial y_o^6(N)}\frac{\partial y_o^6(N)}{\partial y_k^5(N)}\frac{\partial y_k^5(N)}{\partial \psi_k(N)}\right] \times \frac{\partial \psi_k(N)}{\partial w_{ik}^5(N)} = \eta_3 \delta_{ik}^5 \phi_{ik}^5 \quad (31)$$

where η_2 and η_3 are the learning rates. Thus, the updated connective weights w_r^5 and w_{ik}^5 are acquired as

$$w_r^5(N+1) = w_r^5(N) + \Delta w_r^5 \quad (32)$$

$$w_{ik}^5(N+1) = w_{ik}^5(N) + \Delta w_{ik}^5. \quad (33)$$

3) *Petri Layer:* In this layer, the error term is propagated and computed as follows:

$$\delta_p^4 = -\frac{\partial E}{\partial y_p^4} = -\left[\frac{\partial E}{\partial y_o^6(N)}\frac{\partial y_o^6(N)}{\partial y_k^5(N)}\right]\frac{\partial y_k^5(N)}{\partial y_p^4(N)} = \delta_k^5 \psi_k w_k^5 w_r^5 y_k^5(N-1). \quad (34)$$

4) *Rule Layer:* The term of the propagated error is represented in the following:

$$\delta_l^3 = -\frac{\partial E}{\partial y_l^3} = -\left[\frac{\partial E}{\partial y_o^6(N)}\frac{\partial y_o^6(N)}{\partial y_k^5(N)}\frac{\partial y_k^5(N)}{\partial y_p^4(N)}\right]\frac{\partial y_p^4(N)}{\partial y_l^3(N)} = \delta_p^4 t_p^4. \quad (35)$$

5) *Membership Layer:* According to the chain rule, the error term needs to be calculated and propagated as the

following:

$$\begin{aligned}\delta_j^2 &= -\frac{\partial E}{\partial \text{net}_j^2} \\ &= -\left[\frac{\partial E}{\partial y_o^6(N)}\frac{\partial y_o^6(N)}{\partial y_k^5(N)}\frac{\partial y_k^5(N)}{\partial y_p^4(N)}\frac{\partial y_p^4(N)}{\partial y_l^3(N)}\right] \\ &\quad\times \frac{\partial y_l^3(N)}{\partial y_j^2(N)}\frac{\partial y_j^2(N)}{\partial \text{net}_j^2(N)} \\ &= \sum_l \delta_l^3 w_{jl}^3 y_j^2. \end{aligned} \tag{36}$$

The updates of the mean Δm_{ij}^2 and standard deviation $\Delta\sigma_{ij}^2$ of the membership functions are described as follows:

$$\begin{aligned}&\Delta m_{ij}^2 = -\eta_4\frac{\partial E}{\partial m_{ij}^2} = \\ &-\eta_4\left[\frac{\partial E}{\partial y_o^6(N)}\frac{\partial y_o^6(N)}{\partial y_k^5(N)}\frac{\partial y_k^5(N)}{\partial y_p^4(N)}\frac{\partial y_p^4(N)}{\partial y_l^3(N)}\frac{\partial y_l^3(N)}{\partial y_j^2(N)}\frac{\partial y_j^2(N)}{\partial net_j^2(N)}\right]\frac{\partial net_j^2(N)}{\partial m_{ij}^2(N)} \\ &= \eta_4\delta_j^2\frac{2(y_i^1 - m_{ij}^2)}{(\sigma_{ij}^2)^2}\end{aligned} \tag{37}$$

$$\begin{aligned}&\Delta\sigma_{ij}^2 = -\eta_5\frac{\partial E}{\partial \sigma_{ij}^2} = \\ &-\eta_5\left[\frac{\partial E}{\partial y_o^6(N)}\frac{\partial y_o^6(N)}{\partial y_k^5(N)}\frac{\partial y_k^5(N)}{\partial y_p^4(N)}\frac{\partial y_p^4(N)}{\partial y_l^3(N)}\frac{\partial y_l^3(N)}{\partial y_j^2(N)}\frac{\partial y_j^2(N)}{\partial net_j^2(N)}\right]\frac{\partial net_j^2(N)}{\partial \sigma_{ij}^2(N)} \\ &= \eta_5\delta_j^2\frac{2(y_i^1 - m_{ij}^2)^2}{(\sigma_{ij}^2)^3}\end{aligned} \tag{38}$$

where η_4 and η_5 are the learning rates of the mean and standard deviation, respectively. Therefore, the updated mean m_{ij}^2 and standard deviation σ_{ij}^2 of the membership functions are acquired as follows:

$$m_{ij}^2(N+1) = m_{ij}^2(N) + \Delta m_{ij}^2 \tag{39}$$

$$\sigma_{ij}^2(N+1) = \sigma_{ij}^2(N) + \Delta\sigma_{ij}^2. \tag{40}$$

Since there are the uncertainties such as external disturbances and parameter variations in the dynamic storage system, the accurate calculation of the Jacobian of the storage system, $\partial V_{ab,\text{peak}}/\partial y_o^6(N)$, cannot be determined. Therefore, for the purposes of solving this problem and increasing the online learning rate of the network parameters, the delta adaptation law is adopted in the following [7]:

$$\delta_o^6 \cong e + \dot{e}. \tag{41}$$

C. Convergence Analysis of PetriRWFNN Controller

The choice of the learning rates of the proposed PetriRWFNN has a momentous effect on the performance of the network. For the purpose of training the proposed PetriRWFNN effectively, the varied learning rates [30], [31], which pledge the convergence of the voltage control, based on the analysis of a discrete-type Lyapunov function, are detailedly derived in this article. To guarantee the convergence of voltage control, specific learning rate coefficients for the training of the network parameters are obtained from the following convergence analysis.

The error function shown in (24) is considered a discrete-type Lyapunov function. Then, the variation of the Lyapunov function is described in the following:

$$\Delta E(N) = E(N+1) - E(N). \tag{42}$$

Linearized model [31] of the Lyapunov function is obtained via (26), (30), (31), (37), and (38) in the following:

$$\begin{aligned}&E(N+1) = E(N) + \Delta E(N) \\ &\approx E(N) + \sum_{k=1}^{9}\left[\frac{\partial E(N)}{\partial w_k^6}\Delta w_k^6\right] + \sum_{r=1}^{9}\left[\frac{\partial E(N)}{\partial w_r^5}\Delta w_r^5\right] \\ &+ \sum_{k=1}^{9}\sum_{i=1}^{2}\left[\frac{\partial E(N)}{\partial w_{ik}^5}\Delta w_{ik}^5\right] \\ &\quad + \sum_{j=1}^{6}\sum_{i=1}^{2}\left[\frac{\partial E(N)}{\partial m_{ij}^2}\Delta m_{ij}^2 + \frac{\partial E(N)}{\partial \sigma_{ij}^2}\Delta\sigma_{ij}^2\right] \\ &= \tfrac{1}{5}E(N) - \eta_1\sum_{k=1}^{9}\left[\frac{\partial E}{\partial y_o^6(N)}\frac{\partial y_o^6(N)}{\partial w_k^6}\right]^2 \\ &+\tfrac{1}{5}E(N) - \eta_2\sum_{r=1}^{9}\left[\frac{\partial E}{\partial y_k^5(N)}\frac{\partial y_k^5(N)}{\partial w_r^5(N)}\right]^2 \\ &+\tfrac{1}{5}E(N) - \eta_3\sum_{k=1}^{9}\sum_{i=1}^{2}\left[\frac{\partial E}{\partial \psi_k(N)}\frac{\partial \psi_k(N)}{\partial w_{ik}^5(N)}\right]^2 \\ &+\tfrac{1}{5}E(N) - \eta_4\sum_{j=1}^{6}\sum_{i=1}^{2}\left[\frac{\partial E}{\partial net_j^2(N)}\frac{\partial net_j^2(N)}{\partial m_{ij}^2(N)}\right]^2 \\ &+\tfrac{1}{5}E(N) - \eta_5\sum_{j=1}^{6}\sum_{i=1}^{2}\left[\frac{\partial E}{\partial net_j^2(N)}\frac{\partial net_j^2(N)}{\partial \sigma_{ij}^2(N)}\right]^2\end{aligned} \tag{43}$$

where Δw_k^6, Δw_r^5, Δw_{ik}^5, Δm_{ij}^2, and $\Delta\sigma_{ij}^2$ depict the variations of the connect weights, recurrent weights, wavelet weights, the means, and the standard deviations, respectively. If the learning rate coefficients of the proposed PetriRWFNN are designed as

$$\eta_1 = \frac{E(N)}{5\left[\sum_{k=1}^{9}\left(\frac{\partial E}{\partial y_o^6(N)}\frac{\partial y_o^6(N)}{\partial w_k^6}\right)^2 + \varepsilon\right]} \tag{44}$$

$$\eta_2 = \frac{E(N)}{5\left[\sum_{r=1}^{9}\left(\frac{\partial E}{\partial y_k^5(N)}\frac{\partial y_k^5(N)}{\partial w_r^5(N)}\right)^2 + \varepsilon\right]} \tag{45}$$

$$\eta_3 = \frac{E(N)}{5\left[\sum_{k=1}^{9}\sum_{i=1}^{2}\left(\frac{\partial E}{\partial \psi_k(N)}\frac{\partial \psi_k(N)}{\partial w_{ik}^5(N)}\right)^2 + \varepsilon\right]} \tag{46}$$

$$\eta_4 = \frac{E(N)}{5\left[\sum_{j=1}^{6}\sum_{i=1}^{2}\left(\frac{\partial E}{\partial net_j^2(N)}\frac{\partial net_j^2(N)}{\partial m_{ij}^2(N)}\right)^2 + \varepsilon\right]} \tag{47}$$

$$\eta_5 = \frac{E(N)}{5\left[\sum_{j=1}^{6}\sum_{i=1}^{2}\left(\frac{\partial E}{\partial net_j^2}\frac{\partial net_j^2(N)}{\partial \sigma_{ij}^2(N)}\right)^2 + \varepsilon\right]} \tag{48}$$

and ε is a positive constant, (43) can be reformulated as follows:

$$\begin{aligned}E(N+1) &\approx \varepsilon(\eta_1 + \eta_2 + \eta_3 + \eta_4 + \eta_5) \\ &\approx \frac{E(N)\varepsilon}{5\left[\sum_{k=1}^{9}\left(\frac{\partial E}{\partial y_o^6(N)}\frac{\partial y_o^6(N)}{\partial w_k^6}\right)^2 + \varepsilon\right]}\end{aligned}$$

$$+\frac{E(N)\varepsilon}{5\left[\sum_{r=1}^{9}\left(\frac{\partial E}{\partial y_k^5(N)}\frac{\partial y_k^5(N)}{\partial w_r^5(N)}\right)^2+\varepsilon\right]}$$
$$+\frac{E(N)\varepsilon}{5\left[\sum_{k=1}^{9}\sum_{i=1}^{2}\left(\frac{\partial E}{\partial \psi_k(N)}\frac{\partial \psi_k(N)}{\partial w_{ik}^5(N)}\right)^2+\varepsilon\right]}$$
$$+\frac{E(N)\varepsilon}{5\left[\sum_{j=1}^{6}\sum_{i=1}^{2}\left(\frac{\partial E}{\partial \mathrm{net}_j^2(N)}\frac{\partial \mathrm{net}_j^2(N)}{\partial m_{ij}^2(N)}\right)^2+\varepsilon\right]}$$
$$+\frac{E(N)\varepsilon}{5\left[\sum_{j=1}^{6}\sum_{i=1}^{2}\left(\frac{\partial E}{\partial \mathrm{net}_j^2(N)}\frac{\partial \mathrm{net}_j^2(N)}{\partial \sigma_{ij}^2(N)}\right)^2+\varepsilon\right]}$$
$$<\frac{E(N)}{5}+\frac{E(N)}{5}+\frac{E(N)}{5}+\frac{E(N)}{5}+\frac{E(N)}{5}=E(N). \tag{49}$$

Finally, the convergence of the proposed PetriRWFNN controller is guaranteed according to (24) and (49). Therefore, the convergence of the voltage control of the storage system can be pledged.

D. Procedure of Storage Using PetriRWFNN Controller

The flowchart of the storage system using the proposed PetriRWFNN controller for voltage control in islanded mode is illustrated in Fig. 3(b) and represented in the following.

1) *Sampling:* In order to obtain the peak of the line-to-line voltage $V_{ab,\mathrm{peak}}$, the analog three-phase voltages $V_a,\ V_b,\ V_c$ of the microgrid are detected by the voltage sensor circuit and converted to digital signals through an analog-to-digital converter (ADC) in the digital signal processor (DSP). Then, the voltage error $e = V_{ab,\mathrm{peak}}^* - V_{ab,\mathrm{peak}}$ is computed and sent to the proposed PetriRWFNN controller.
2) *Input Layer:* The node inputs of this layer are $x_1^1 = e(t)$ and its derivative $x_2^1 = \dot{e}(t)$. The node outputs $y_i^1(N)$ are sent to the membership layer.
3) *Membership Layer:* To implement the fuzzification operation, each node in this layer utilizes the Gaussian function and the outputs $y_j^2(N)$ are sent to the rule layer.
4) *Rule Layer:* Each node in this layer multiplies the input signals and outputs the result of the product. The outputs $y_l^3(N)$ are sent to the Petri layer.
5) *Petri Layer:* The Petri layer of the proposed PetriRWFNN to generate tokens makes use of competition laws to select suitable fired nodes. The node outputs $y_p^4(N)$ are computed and sent to the wavelet and consequent layer.
6) *Wavelet and Consequent Layer:* The wavelet function and the recurrent property of RNN are implemented in this layer. The nodes in this layer multiply the output signals from the Petri layer, wavelet function, and recurrent property, and output the result of the product. The outputs are $y_k^5(N)$ and sent to the output layer.
7) *Output Layer:* The summation operation is performed in this layer and the output is calculated as $y_o^6(N)$. Meanwhile, the output $y_o^6(N)$ of the proposed PetriRWFNN is the q-axis current command i_{sq}^* of the storage system operated in an islanded mode for voltage control shown in Fig. 2(a).
8) *Online Network Parameters Learning:* The online parameters learning is achieved by online tuning of the connective weights w_k^6 between the output layer and the wavelet and consequent layer, the recurrent weights w_r^5, the connective weights w_{ik}^5 in the wavelet function, and the mean m_{ij}^2 and standard deviations σ_{ij}^2 of the membership functions in the membership layer using the BP algorithm.

IV. Experimental Results

In this article, the ac microgrid using master/slave control is developed. The microgrid is composed of the storage system, PV system and loads, and can be operated in either grid-connected mode or islanded mode. The block diagrams of the designed DSP-based storage system and personal computer (PC)-based PV system are provided in Fig. 4(a) and (b), respectively. In the block diagram of the DSP-based storage system shown in Fig. 4(a), the control algorithms of the storage system, including the PLL, active and reactive power controls, presynchronization estimation, voltage and frequency control, and the proposed PetriRWFNN, are performed by the DSP TMS320F28335 with 1 ms sampling time. The switching frequency of the DSP-based storage system is 16 kHz. Moreover, the peripheral circuits of the storage system comprise the interlocking, protection, voltage, and current feedback circuits. In this article, the LiFePo4 battery, which is composed of six battery packs in series, is adopted as the storage system. Each battery pack of the LiFePo4 battery comprises 24 battery cells with 12 cells in series as a unit and two units in parallel. The capacity and the nominal voltage of the battery storage, the battery cell, and the battery pack are 30 Ah/237.6 V, 15 Ah/3.3 V, and 30 Ah/39.6 V; the cut-off discharge voltage, the recommended charging voltage, and the balance voltage of the battery cell are 2.5 V, 3.5 V, and 3.5 V, respectively. Furthermore, the block diagram of the PC-based PV system is illustrated in Fig. 4(b). The MATLAB and Simulink real-time control package with 0.5 ms sampling time is adopted to implement the control algorithm of the PV system. The peripheral circuits of the PV system consist of the protection, voltage, and current feedback circuits. The detected three-phase voltages $V_a,\ V_b,\ V_c$ of the microgrid and the three-phase currents $i_{su},\ i_{sv},\ i_{sw}$ of the PV system are transmitted to the PC through the A/D converter on the PCI-1716 interface card for the synchronization and active/reactive power control. The switching frequency of the PV system is 10 kHz. In this article, a Chroma 62150H-6005 is adopted to emulate the PV panel. In addition, the short-circuit current and open-circuit voltage of the emulated PV panel are 5.632 A and 377.4 V, respectively; the current, voltage, and power output of the maximum power point

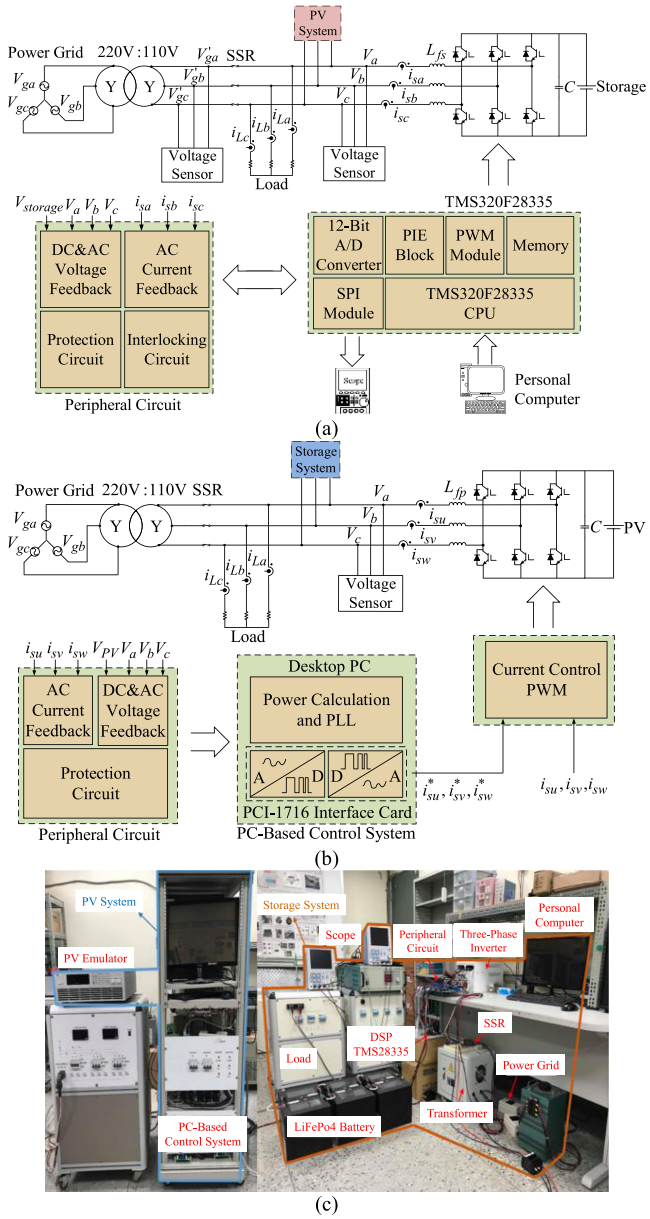

Fig. 4. AC microgrid using master/slave control. (a) Block diagram of the DSP-based storage system. (b) Block diagram of the PC-based PV system. (c) Photograph of the experimental setup.

of the PV panel are 5.556 A, 360 V, and 2 kW, respectively. The photo of the storage and PV systems is represented in Fig. 4(c).

Due to the transient deterioration in voltage and active power output of the microgrid system during the mode switching [9], [10], the novel PetriRWFNN controller is proposed in this article to improve the transient responses of the voltage and active power of the microgrid. Hence, in order to confirm the effectiveness of the storage system using the proposed PetriRWFNN for the voltage control, active power control, and the presynchronization estimation, three test scenarios are designed as follows in the experimentation: 1) switching from grid-connected mode to islanded mode; 2) grid reconnection from islanded mode to grid-connected mode with phase difference 90° between the voltage of the islanded microgrid and the voltage of the power grid; and 3) grid reconnection with phase difference 180° between the voltage of the islanded microgrid and the voltage of the power grid. Moreover, the experimental results using PI- and FNN-controlled storage systems of the microgrid are also provided for comparison.

The experimental results of the microgrid switching from grid-connected mode to islanded mode are demonstrated. In this scenario, the microgrid with 2 kW load operates in a grid-connected mode in the interval 0–10 s and in the islanded mode in the interval 10–20 s owing to the power grid fail at 10 s. In the grid-connected mode, the active and reactive power controls are adopted in both the storage system and PV system. The active power command P_s^* and reactive power command Q_s^* of the storage system are set to be 1 kW and 0 Var, respectively. The active power command P_p^* and reactive power command Q_p^* of the PV system are set to be 0.7 kW and 0 Var. Moreover, when the power grid interrupts at 10 s, the control algorithm of the storage system changes from mode I to II, as shown in Fig. 2(a), to implement the voltage and frequency control for maintaining the voltage and frequency of the microgrid due to the absence of the power grid. The peak value of the line-to-line voltage command $V_{ab,\mathrm{peak}}^*$ and the frequency command f^* of the storage system are set to be 155 V and 60 Hz. Meanwhile, the active power command P_p^* and reactive power command Q_p^* of the PV system are still set to be 0.7 kW and 0 Var in the islanded mode. First, the experimental results of the microgrid using the PI controller are provided in Fig. 5(a)–(d). The responses of the active power and reactive power of the storage system using the traditional PI controller are illustrated in Fig. 5(a). The responses of the active power and reactive power of the PV system and power grid are provided in Fig. 5(b) and (c). The responses of the voltage and frequency of the microgrid using the traditional PI controller and the output current i_{sa} of the storage system in the interval 9.5–10.5 s are represented in Fig. 5(d). From the experimental results of the storage system using the PI controller shown in Fig. 5(a)–(c), since the microgrid is equipped with 2 kW load and the active power commands P_s^* and P_p^* of the storage and PV systems are set to be 1 kW and 0.7 kW respectively in grid-connected mode, the power grid delivers 0.3 kW power energy to the load in the interval 0–10 s for balancing the supply and demand. When the power grid fails at 10 s, the operation mode of the storage system is changed from mode I to mode II to maintain the voltage and frequency of the microgrid. Although the storage system adopts the voltage and frequency control in the islanded mode in the interval 10–20 s, the storage system still dispatches 1.3 kW to the 2 kW load for the power balance of supply and demand due to the absence of the power grid. Furthermore, according to Fig. 5(d) in the interval 9.5–10.5 s, the steady-state responses of the voltage and frequency of the microgrid are maintained corresponding to the voltage and frequency commands of the storage system. However, the transient responses of the voltage of the microgrid and the output current i_{sa} of the storage system are sluggish at 10 s. Consequently, the transient deterioration in active power output of the storage system is obvious at 10 s, as shown in Fig. 5(a), due to the poor property of the PI controller. Then, the

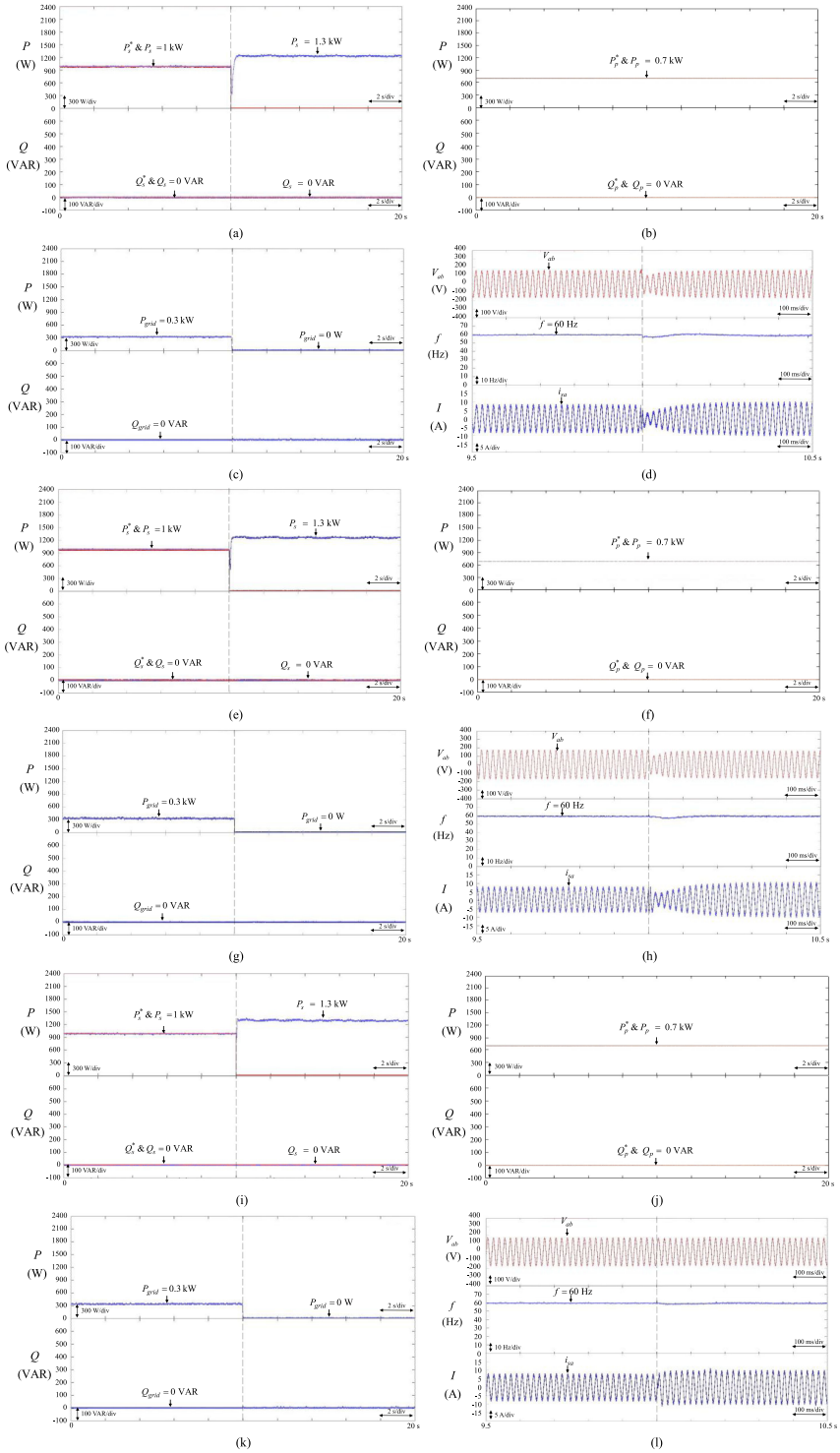

Fig. 5. Microgrid switching from grid-connected mode to islanded mode. (a) Responses of active power and reactive power of storage system using the PI controller. (b) Responses of active power and reactive power of PV system. (c) Responses of active power and reactive power of power grid. (d) Responses of voltage and frequency of microgrid using the PI controller and output current of the storage system in the interval 9.5–10.5 s. (e) Responses of active power and reactive power of storage system using FNN controller. (f) Responses of active power and reactive power of PV system. (g) Responses of active power and reactive power of power grid. (h) Responses of voltage and frequency of microgrid using FNN controller and output current of the storage system in the interval 9.5–10.5 s. Microgrid switching from grid-connected mode to islanded mode. (i) Responses of active power and reactive power of storage system using the proposed PetriRWFNN controller. (j) Responses of active power and reactive power of PV system. (k) Responses of active power and reactive power of power grid. (l) Responses of voltage and frequency of microgrid using the proposed PetriRWFNN controller and output current of the storage system in the interval 9.5–10.5 s.

experimental results of the microgrid using the FNN controller are provided in Fig. 5(e)–(h). The responses of the active power and reactive power of the storage system using the FNN controller are illustrated in Fig. 5(e). The responses of the active power and reactive power of the PV system and power grid are provided in Fig. 5(f) and (g). The responses of the voltage and frequency of the microgrid using the FNN controller and the output current i_{sa} of the storage system in the interval 9.5–10.5 s are represented in Fig. 5(h). According to the experimental results using the FNN controller, the power balance of supply and demand can be achieved in both grid-connected mode and islanded mode shown in Fig. 5(e)–(g). In addition, the transient responses of the voltage of the microgrid and the output current i_{sa} of the storage system using the FNN controller are slightly improved at 10 s, as shown in Fig. 5(h). Hence, the transient deterioration in active power output of the storage system is still obvious at 10 s, as shown in Fig. 5(e). In order to improve the transient responses of the microgrid system during the mode switching, the novel PetriRWFNN controller is proposed to substitute the PI and FNN controllers in the q-axis current command i_{sq}^{*} of the storage system, as shown in Fig. 2(a). The experimental results of the microgrid using the proposed PetriRWFNN controller are provided in Fig. 5(i)–(l). The responses of the active power and reactive power of the storage system using the proposed PetriRWFNN controller are illustrated in Fig. 5(i). The responses of the active power and reactive power of the PV system and power grid are provided in Fig. 5(j) and (k). The responses of the voltage and frequency of the microgrid using the proposed PetriRWFNN controller and the output current i_{sa} of the storage system in the interval 9.5–10.5 s are represented in Fig. 5(l). From the experimental results of the storage system using the proposed PetriRWFNN controller, as shown in Figs. 5(i)–(k), the power balance of supply and demand is also achieved in both grid-connected and islanded modes of the microgrid. In addition, since the proposed PetriRWFNN controller is composed of the FNN, WNN, RNN, and PN, the proposed PetriRWFNN owns the abilities of FNN in generalization, self-learning and coping with the uncertain nonlinear system, the capabilities of WNN in fault tolerance, approximation, and quick convergence, the memory characteristic of RNN, and the mathematical modeling abilities of PN. Comparing with the experimental result using the PI and FNN controllers, as shown in Fig. 5(a) and (e), the transient response of the active power output of the storage system using the proposed PetriRWFNN controller is better than the experimental result using the PI and FNN controllers at 10 s, as shown in Fig. 5(i). Consequently, the transient responses of the voltage of the microgrid and the current i_{sa} of the storage system using the proposed PetriRWFNN controller are much improved at 10 s, as shown in Fig. 5(d), (h), and (l), due to the powerful property of the proposed PetriRWFNN controller. Therefore, the performance of the seamless switching of the microgrid is proved by using the proposed PetriRWFNN controller.

To verify the feasibility of the proposed presynchronization estimation, the experimental results of the islanded microgrid to reconnect with the power grid with a phase difference of 90° between the voltage of the islanded microgrid and the voltage of the power grid are demonstrated. In this scenario, the microgrid with a 2 kW load initially operates in islanded mode. In islanded mode, the storage system adopts the voltage and frequency control. When the microgrid reconnects with the power grid, the active and reactive power controls are adopted in the storage system. The active power command P_s^{*} and reactive power command Q_s^{*} of the storage system operated in grid-connected mode are set to be 0.5 kW and 0 Var, respectively. The active power command P_p^{*} and reactive power command Q_p^{*} of the PV system are set to be 1 kW and 0 Var in both islanded and grid-connected modes. The experimental results of the islanded microgrid using PI controller are provided in Fig. 6(a)–(d). The responses of line-to-line voltages V'_{gab} and V_{ab} of the power grid and microgrid, frequency of the microgrid, and the output current i_{sa} of the storage system are illustrated in Fig. 6(a). The responses of the active and reactive powers of the storage system using the conventional PI controller, PV system, and power grid are shown in Fig. 6(b)–(d). From the experimental results, as shown in Fig. 6(a), when the microgrid initially operates in islanded mode and the power grid returns to normal operation, the islanded microgrid cannot reconnect with the power grid due to the phase difference of 90° of the voltage. Thus, the proposed presynchronization estimation of the storage system starts at 0.2 s to synchronize with the power grid. When the line-to-line voltages V'_{gab} and V_{ab} of the power grid and microgrid are synchronous at 0.36 s, the grid-reconnection of the microgrid is performed and the operation mode of the storage system is changed from mode II to mode I to control the active and reactive power outputs, as shown in Fig. 2(a). Therefore, the proposed presynchronization estimation and the seamless switching are successfully implemented and effective. Moreover, according to Fig. 6(a)–(d), although the storage system adopts the voltage and frequency control in islanded mode, the storage system still dispatches 1 kW to the 2 kW load for the power balance of supply and demand due to the absence of the power grid. When the microgrid reconnects with the power grid, the active and reactive power outputs of the storage system accurately track the active and reactive power commands 0.5 kW and 0 Var and the power grid delivers 0.5 kW power energy to the 2 kW, as shown in Fig. 6(b) and (d), for balancing the supply and demand. Hence, the power balance of supply and demand can be achieved in both islanded and grid-connected modes. However, when the islanded microgrid reconnects with the power grid during the mode switching, the transient response of the active power output of the storage system fluctuates due to the PI-controlled storage system, as shown in Fig. 6(b). Furthermore, the experimental results of the islanded microgrid using the FNN controller are provided in Fig. 6(e)–(h). The responses of line-to-line voltages V'_{gab} and V_{ab} of the power grid and microgrid, frequency of the microgrid, and the output current i_{sa} of the storage system are illustrated in Fig. 6(e). The responses of the active and reactive powers of the storage system using the FNN controller, PV system, and power grid are shown in Fig. 6(f)–(h). According to the experimental results as shown in Fig. 6(e)–(h), the proposed presynchronization estimation of the storage system using the FNN controller is also successfully implemented and the power balance of supply and demand can also be obtained in both islanded and grid-connected modes. Then, the transient response

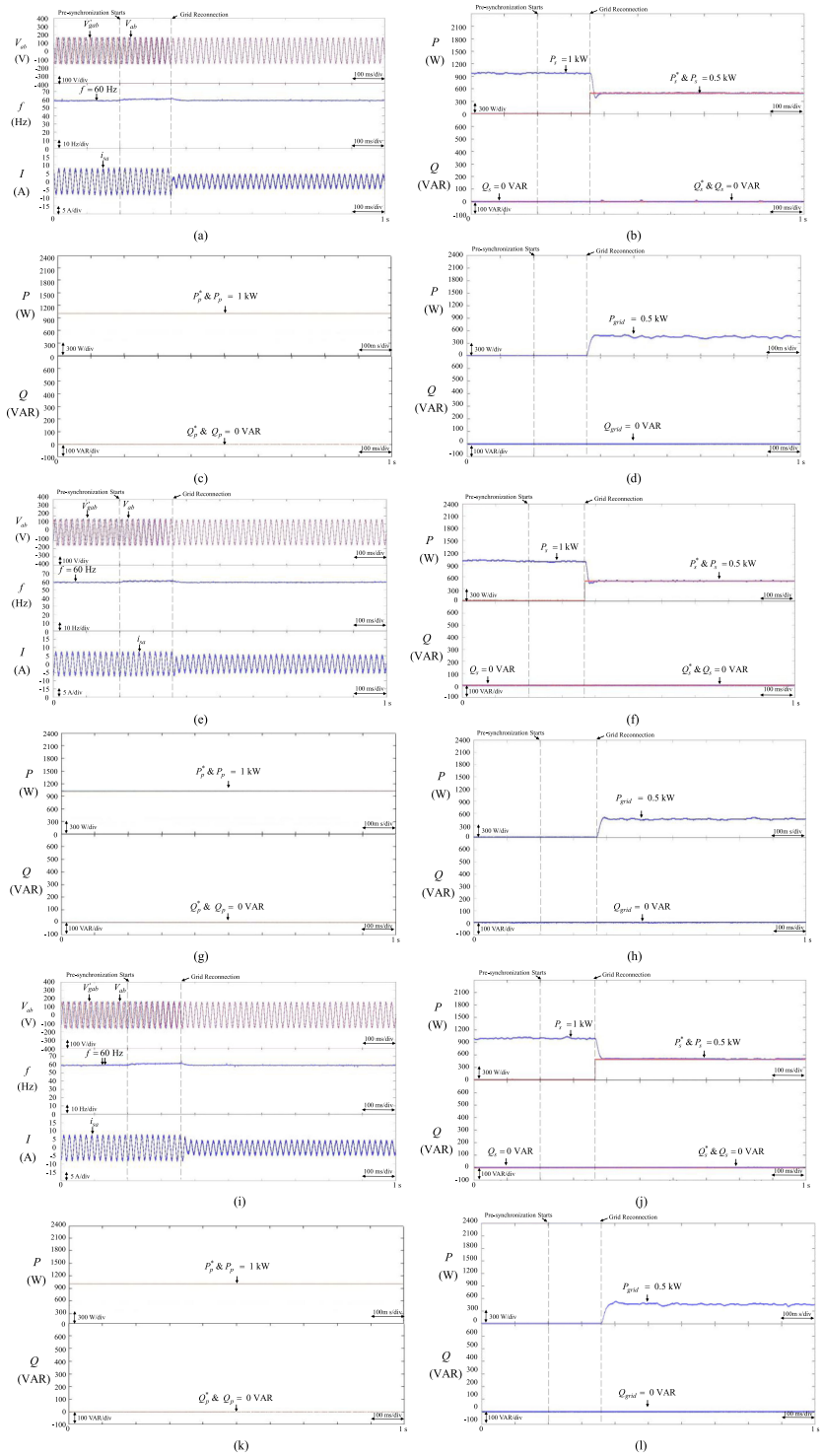

Fig. 6. Grid reconnection of islanded microgrid with phase difference 90°. (a) Responses of line-to-line voltages of power grid and microgrid, frequency of microgrid, and output current of the storage system using the PI controller. (b) Responses of active power and reactive power of storage system using the PI controller. (c) Responses of active power and reactive power of PV system. (d) Responses of active power and reactive power of power grid. (e) Responses of line-to-line voltages of power grid and microgrid, frequency of microgrid, and output current of the storage system using FNN controller. (f) Responses of active power and reactive power of storage system using FNN controller. (g) Responses of active power and reactive power of PV system. (h) Responses of active power and reactive power of power grid. Grid reconnection of islanded microgrid with phase difference 90°. (i) Responses of line-to-line voltages of power grid and microgrid, frequency of microgrid, and output current of the storage system using the proposed PetriRWFNN controller. (j) Responses of active power and reactive power of storage system using the proposed PetriRWFNN controller. (k) Responses of active power and reactive power of PV system. (l) Responses of active power and reactive power of power grid.

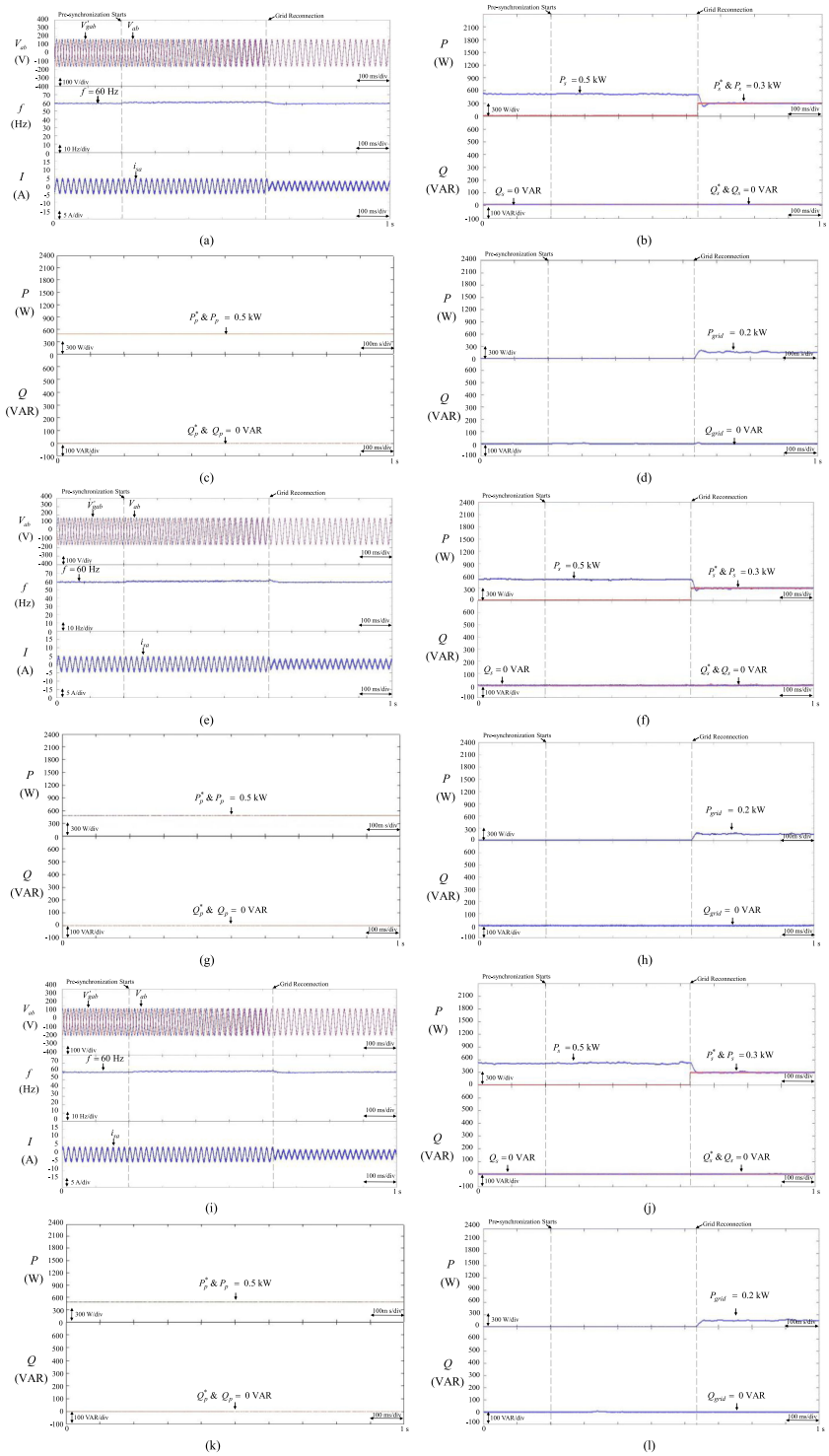

Fig. 7. Grid reconnection of islanded microgrid with phase difference 180°. (a) Responses of line-to-line voltages of power grid and microgrid, frequency of microgrid, and output current of the storage system using the PI controller. (b) Responses of active power and reactive power of storage system using the PI controller. (c) Responses of active power and reactive power of PV system. (d) Responses of active power and reactive power of power grid. (e) Responses of line-to-line voltages of power grid and microgrid, frequency of microgrid, and output current of the storage system using FNN controller. (f) Responses of active power and reactive power of storage system using FNN controller. (g) Responses of active power and reactive power of PV system. (h) Responses of active power and reactive power of power grid. Grid reconnection of islanded microgrid with phase difference 180°. (i) Responses of line-to-line voltages of power grid and microgrid, frequency of microgrid, and output current of the storage system using the proposed PetriRWFNN controller. (j) Responses of active power and reactive power of storage system using the proposed PetriRWFNN controller. (k) Responses of active power and reactive power of PV system. (l) Responses of active power and reactive power of power grid.

of the active power output of the storage system is slightly improved during the mode switching shown in Fig. 6(f). In addition, the experimental results of the islanded microgrid using the proposed PetriRWFNN controller are provided in Fig. 6(i)–(l). The responses of line-to-line voltages V'_{gab} and V_{ab} of the power grid and microgrid, frequency of the microgrid, and the output current i_{sa} of the storage system are illustrated in Fig. 6(i). The responses of the active and reactive powers of the storage system using the proposed PetriRWFNN controller, PV system, and power grid are illustrated in Fig. 6(k)–(l). According to the experimental results shown in Fig. 6(i)–(l), the proposed presynchronization estimation of the storage system using the proposed PetriRWFNN controller is also successfully implemented and the power balance of supply and demand can also be obtained in both islanded and grid-connected modes. Comparing with the experimental results using the PI- and FNN-controlled storage systems, the transient response of the active power of the storage system using the proposed PetriRWFNN controller is effectively improved during the mode switching, as shown in Fig. 6(b), (f), and (j), owing to the online learning ability of the proposed PetriRWFNN controller and the ability to deal with the time-varying inputs or outputs. Finally, the experimental results of the islanded microgrid to reconnect with power grid with phase difference 180° are demonstrated. In this case, the microgrid with 1 kW load initially operates in islanded mode. In islanded mode, the storage system adopts the voltage and frequency control. The active power command P_s^* and reactive power command Q_s^* of the storage system operated in grid-connected mode are set to be 0.3 kW and 0 Var, respectively. The active power command P_p^* and reactive power command Q_p^* of the PV system are set to be 0.5 kW and 0 Var in both islanded and grid-connected modes. The experimental results of the islanded microgrid using PI controller are provided in Fig. 7(a)–(d). The responses of line-to-line voltages V'_{gab} and V_{ab} of the power grid and microgrid, frequency of the microgrid, and the output current i_{sa} of the storage system are illustrated in Fig. 7(a). The responses of the active and reactive powers of the storage system using the conventional PI controller, PV system, and power grid are shown in Fig. 7(b)–(d). Then, the experimental results of the islanded microgrid using the FNN controller are provided in Fig. 7(e)–(h). The responses of line-to-line voltages V'_{gab} and V_{ab} of the power grid and microgrid, frequency of the microgrid, and the output current i_{sa} of the storage system using FNN controller are illustrated in Fig. 7(e). The responses of the active and reactive powers of the storage system using FNN controller, PV system, and power grid are shown in Fig. 7(f)–(h). In addition, the experimental results of the islanded microgrid using the proposed PetriRWFNN controller are illustrated in Fig. 7(i)–(l). From the experimental results, as shown in Fig. 7(a), (e), and (i), when the microgrid initially operates in islanded mode and the power grid returns to normal operation, the islanded microgrid cannot reconnect with the power grid due to the phase difference of 180° of the voltage. Thus, the proposed presynchronization estimation of the storage system starts at 0.2 s to synchronize with the power grid. When the line-to-line voltages V'_{gab} and V_{ab} of the power grid and microgrid are synchronous at 0.63 s, the grid-reconnection of the microgrid is performed and the operation mode of the storage system is changed to control the active and reactive power outputs. Thus, the proposed presynchronization estimation and the seamless switching are also successfully implemented and effective. Additionally, the power balance of supply and demand can also be obtained in both islanded and grid-connected modes, no matter what the PI, FNN, or the proposed PetriRWFNN controller is adopted in the storage system. However, compared to the PI- and FNN-controlled storage systems, the transient response of the active power of the storage system using the proposed PetriRWFNN controller is effectively improved during the mode switching, as shown in Fig. 7(b), (f), and (j), owing to the powerful robust ability and online learning ability of the proposed PetriRWFNN controller.

TABLE I
COMPUTE TIME OF STORAGE SYSTEM USING PI, FNN, AND PROPOSED PETRIRWFNN CONTROLLERS

Controllers	PI	FNN	Proposed PetriRWFNN
Total Operation Cycles	173	2477	8832
Execution Time	1.153 us	16.513 us	58.88 us

In this article, the compute or training time of the "C" program in the TMS320F28335 32-bit floating-point DSP with 150 MHz can be obtained by the clock tool of Texas Instruments Code Composer Studio v6 program editing interface. The total operation cycles and total execution time of the PI, FNN, and the proposed PetriRWFNN-controlled storage system switching from grid-connected mode to islanded mode are compared in Table I. The total operation cycles and total execution time for the proposed PetriRWFNN are 8832 cycles and 58.88 μs, respectively. In consequence, the total execution time of the storage system using the proposed PetriRWFNN controller is still less than 1 ms, which is the sampling interval of the control loop.

V. CONCLUSION

A microgrid has been successfully developed and implemented in this article. The microgrid using the master/slave control consists of a storage system, PV system and loads, and can be operated in either grid-connected mode or islanded mode. Since the different control algorithm is adopted in the master DG at different operation modes, the transient deterioration in voltage and active power output of the microgrid system is obvious during the mode switching. Hence, in order to achieve the seamless switching of microgrids, a novel PetriRWFNN controller is proposed to replace the conventional PI controller for improving the transient responses of the voltage and active power of the microgrid. Moreover, a simple and fast presynchronization estimation for grid reconnection during the switching from the islanded mode to the grid-connected mode is also proposed in this article. Furthermore, the feasibility and the effectiveness of the microgrid using the proposed PetriRWFNN controller are verified by the experimental results. In accordance with the experimental results, the transient responses of the voltage and active power of the microgrid using the proposed PetriRWFNN controller are effectively improved during the

mode switching comparing with the PI and FNN controllers. Moreover, the seamless switching and the grid reconnection of the microgrid using the proposed PetriRWFNN controller are verified due to the online learning ability and powerful robust ability of the proposed PetriRWFNN controller.

The major contributions of this article are as follows:

1) the successful development of a microgrid using master/slave control;
2) the successful development of the proposed online trained PetriRWFNN controller;
3) the successful implementation of the microgrid using the proposed PetriRWFNN controller for the improvements of voltage control, active power control, seamless switching, and grid reconnection of the microgrid.

REFERENCES

[1] K. Yu, Q. Ai, S. Wang, J. Ni, and T. Lv, "Analysis and optimization of droop controller for microgrid system based on small-signal dynamic model," *IEEE Trans. Smart Grid*, vol. 7, no. 2, pp. 695–705, Mar. 2016.

[2] K. H. Tan, F. J. Lin, C. M. Shih, and C. N. Kuo, "Intelligent control of microgrid with virtual inertia using recurrent probabilistic wavelet fuzzy neural network," *IEEE Trans. Power Electron.*, vol. 35, no. 7, pp. 7451–7464, Jul. 2020.

[3] K. H. Tan, F. J. Lin, C. Y. Tsai, and Y. R. Chang, "A distribution static compensator using a CFNN-AMF controller for power quality improvement and dc-link voltage regulation," *Energies*, vol. 11, no. 8, pp. 1–17, Aug. 2018.

[4] D. Gregoratti and J. Matamoros, "Distributed energy trading: The multiple-microgrid case," *IEEE Trans. Ind. Electron.*, vol. 62, no. 4, pp. 2551–2559, Apr. 2015.

[5] J. Lee, J. Guo, J. K. Choi, and M. Zukerman, "Distributed energy trading in microgrids: A game-theoretic model and its equilibrium analysis," *IEEE Trans. Ind. Electron.*, vol. 62, no. 6, pp. 3524–3533, Jun. 2015.

[6] A. Gupta, S. Doolla, and K. Chatterjee, "Hybrid ac–dc microgrid: Systematic evaluation of control strategies," *IEEE Trans. Smart Grid*, vol. 9, no. 4, pp. 3830–3843, Jul. 2018.

[7] K. H. Tan, F. J. Lin, J. H. Chen, and Y. R. Chang, "Intelligent controlled shunt active power filter for voltage and current harmonic compensation in microgrid system," *J. Chin. Inst. Eng.*, vol. 41, no. 4, pp. 269–285, May 2018.

[8] Y. Han, K. Zhang, H. Li, E. A. A. Coelho, and J. M. Guerrero, "MAS-based distributed coordinated control and optimization in microgrid and microgrid clusters: A comprehensive overview," *IEEE Trans. Power Electron.*, vol. 33, no. 8, pp. 6488–6508, Aug. 2018.

[9] S. Chandak, P. Bhowmik, and P. K. Rout, "Dual-stage cascaded control to resynchronise an isolated microgrid with the utility," *IET Renew. Power Gener.*, vol. 14, no. 5, pp. 871–880, Apr. 2020.

[10] X. Tang, W. Deng, and Z. Qi, "Investigation of the dynamic stability of microgrid," *IEEE Trans. Power Syst.*, vol. 29, no. 2, pp. 698–706, Mar. 2014.

[11] I. J. Balaguer, Q. Lei, S. Yang, U. Supatti, and F. Z. Peng, "Control for grid-connected and intentional islanding operations of distributed power generation," *IEEE Trans. Ind. Electron.*, vol. 58, no. 1, pp. 147–157, Jan. 2011.

[12] S. A. Taher, M. Zolfaghari, C. Cho, M. Abedi, and M. Shahidehpour, "A new approach for soft synchronization of microgrid using robust control theory," *IEEE Trans. Power Del.*, vol. 32, no. 3, pp. 1370–1381, Jun. 2017.

[13] S. Shah, H. Sun, D. Nikovski, and J. Zhang, "VSC-based active synchronizer for generators," *IEEE Trans. Energy Convers.*, vol. 33, no. 1, pp. 116–125, Mar. 2018.

[14] K. H. Tan, "Squirrel-cage induction generator system using wavelet Petri fuzzy neural network control for wind power applications," *IEEE Trans. Power Electron.*, vol. 31, no. 7, pp. 5242–5254, Jul. 2016.

[15] K. H. Tan, F. J. Lin, and J. H. Chen, "DC-Link voltage regulation using RPFNN-AMF for three-phase active power filter," *IEEE Access*, vol. 6, no. 1, pp. 37454–37463, Jun. 2018.

[16] C. Sun, H. Gao, W. He, and Y. Yu, "Fuzzy neural network control of a flexible robotic manipulator using assumed mode method," *IEEE Trans. Neural Netw. Learn. Syst.*, vol. 29, no. 11, pp. 5214–5227, Nov. 2018.

[17] A. Rubaai and P. Young, "Hardware/software implementation of fuzzy-neural-network self-learning control methods for brushless dc motor drives," *IEEE Trans. Ind. Appl.*, vol. 5, no. 1, pp. 414–424, Feb. 2016.

[18] X. Yu, Y. Fu, P. Li, and Y. Zhang, "Fault-tolerant aircraft control based on self-constructing fuzzy neural networks and multivariable SMC under actuator faults," *IEEE Trans. Fuzzy Syst.*, vol. 26, no. 4, pp. 2324–2335, Aug. 2018.

[19] Q. Zhang and A. Benveniste, "Wavelet networks," *IEEE Trans. Neural Netw.*, vol. 3, no. 6, pp. 889–898, Nov. 1992.

[20] F. Duan and L. Dai, "Recognizing the gradual changes in sEMG characteristics based on incremental learning of wavelet neural network ensemble," *IEEE Trans. Ind. Electron.*, vol. 64, no. 5, pp. 4276–4286, May 2017.

[21] F. F. M. El-Sousy and K. A. Abuhasel, "Adaptive nonlinear disturbance observer using a double-loop self-organizing recurrent wavelet neural network for a two-axis motion control system," *IEEE Trans. Ind. Appl.*, vol. 54, no. 1, pp. 764–786, Feb. 2018.

[22] W. R. Yang, C. S. Wang, and C. P. Chen, "Motion-pattern recognition system using a wavelet-neural network," *IEEE Trans. Consum. Electron.*, vol. 65, no. 2, pp. 170–178, May 2019.

[23] R. Zurawski and M. Zhou, "Petri nets and industrial applications: A tutorial," *IEEE Trans. Ind. Electron.*, vol. 41, no. 6, pp. 567–583, Dec. 1994.

[24] K. H. Tan, F. J. Lin, and J. H. Chen, "A three-phase four-leg inverter-based active power filter for unbalanced current compensation using a Petri probabilistic fuzzy neural network," *Energies*, vol. 10, no. 12, pp. 1–21, Dec. 2017.

[25] Y. T. Liu, Y. Y. Lin, S. L. Wu, C. H. Chuang, and C. T. Lin, "Brain dynamics in predicting driving fatigue using a recurrent self-evolving fuzzy neural network," *IEEE Trans. Neural Netw. Learn. Syst.*, vol. 27, no. 2, pp. 347–360, Feb. 2016.

[26] T. de Bruin, K. Verbert, and R. Babuška, "Railway track circuit fault diagnosis using recurrent neural networks," *IEEE Trans. Neural Netw. Learn. Syst.*, vol. 28, no. 3, pp. 523–533, Mar. 2017.

[27] N. McLaughlin, J. M. del Rincon, and P. Miller, "Video person re-identification for wide area tracking based on recurrent neural networks," *IEEE Trans. Circuits Syst. Video Technol.*, vol. 29, no. 9, pp. 2613–2626, Sep. 2019.

[28] J. Xu, R. Rahmatizadeh, L. Bölöni, and D. Turgut, "Real-time prediction of taxi demand using recurrent neural networks," *IEEE Trans. Intell. Transp. Syst.*, vol. 19, no. 8, pp. 2572–2581, Aug. 2018.

[29] R. J. Wai and Y. W. Lin, "Adaptive moving-target tracking control of a vision-based mobile robot via a dynamic Petri recurrent fuzzy neural network," *IEEE Trans. Fuzzy Syst.*, vol. 21, no. 4, pp. 688–701, Aug. 2013.

[30] S. J. Yoo, Y. H. Choi, and J. B. Park, "Generalized predictive control based on self-recurrent wavelet neural network for stable path tracking of mobile robots: Adaptive learning rates approach," *IEEE Trans. Circuits Syst. I, Reg. Paper*, vol. 53, no. 6, pp. 1381–1395, Jun. 2006.

[31] R. J. Wai and C. M. Li, "Design of dynamic Petri recurrent fuzzy neural network and its application to path-tracking control of nonholonomic mobile robot," *IEEE Trans. Ind. Electron.*, vol. 56, no. 7, pp. 2667–2683, Apr. 2009.

Kuang-Hsiung Tan received the B.S., M.S., and Ph.D. degrees in electrical and electronic engineering from the Chung Cheng Institute of Technology (CCIT), National Defense University (NDU), Taoyuan, Taiwan, in 2002, 2007, and 2013, respectively.

He has been a member of the Faculty at CCIT, where he is currently an Associate Professor with the Department of Electrical and Electronic Engineering. His teaching and research interests include power electronics, power quality, microgrid systems, and intelligent control.

Tzu-Yu Tseng received the B.S. degree in electronic engineering from the National Formosa University, Yunlin County, Taiwan, in 2019, and the M.S. degree in electrical engineering from the National Central University, Chungli, Taiwan, in 2021.

His research interests include microgrid systems, storage systems, PV systems, and intelligent control.